

Fireside Corrosion of Alumina-Forming Austenitic (AFA) Stainless Steels

B. S. Lutz¹ · N. M. Yanar² · G. R. Holcomb³ ·
G. H. Meier² 

Received: 13 August 2016 / Revised: 15 November 2016 / Published online: 23 December 2016
© Springer Science+Business Media New York 2016

Abstract The performance of four alumina-forming austenitic alloys was tested in simulative fireside corrosion atmospheres. The alloys were exposed at 700 °C to gas atmospheres of oxygen with varying amounts of SO₂ with two deposits, one which contained Na₂SO₄/K₂SO₄/Fe₂O₃ in a 1.5:1.5:1.0 molar ratio (SCM) and the other Na₂SO₄/K₂SO₄ in a 1:1 molar ratio (M1). The specimens were placed into alumina crucibles and submerged halfway in the powder deposits. Corrosion first initiated in the region where the deposit was thinnest. In the SCM, most alloys exhibited two-stage kinetics: an initiation stage during which degradation was slow followed by a propagation stage during which degradation was rapid. Exposures in the SCM deposit showed a significant effect of alloy composition and microstructure. In the as-processed state, OC4 suffered severe scale spallation and was not protective, while OC8, which contains a higher Cr content, remained protective. The exposures with the various microstructures indicate the significance of the factor on fireside corrosion. The OC8 alloy was extremely resistant in the as-processed state but was

Disclaimer This report was prepared as an account of work sponsored by an agency of the US Government. Neither the US Government nor any agency thereof, nor any of their employees, makes any warranty, express or implied, or assumes any legal liability or responsibility for the accuracy, completeness, or usefulness of any information, apparatus, product, or process disclosed, or represents that its use would not infringe privately owned rights. Reference herein to any specific commercial product, process, or service by trade name, trademark, manufacturer, or otherwise does not necessarily constitute or imply its endorsement, recommendation, or favoring by the US Government or any agency thereof. The views and opinions of authors expressed herein do not necessarily state or reflect those of the US Government or any agency thereof.

✉ G. H. Meier
ghmeier@pitt.edu

¹ University of California, Santa Barbara, Santa Barbara, CA, USA

² Mechanical and Materials Engineering Department, Benedum Engineering Hall Pittsburgh, University of Pittsburgh, Pittsburgh, PA 15261, USA

³ National Energy Technology Laboratory, Albany, OR 97321, USA

rapidly degraded when the microstructure had been equilibrated prior to exposure. Conversely, the OCS and OCT alloys, which were borderline in the as-processed state were quite resistant after their microstructures had been equilibrated. The results indicate that corrosion resistance in these environments comes from alumina, but the alloys need more Cr and in a very accessible microstructure location to get the third-element effect to promote the alumina. The weight changes and the amount of degradation were more severe with M1 than with the SCM. There was more corrosion when the alkali iron trisulfates must be formed from a thermally grown iron oxide scale, than when the iron oxide was already in the deposit. In the latter case, the rate of degradation by “synergistic fluxing” was reduced.

Keywords AFA alloys · Fireside corrosion · Alumina · Chromia · Sigma phase

Introduction

Fireside corrosion occurs in the heat exchanger components of coal-fired power plants by gas phase oxidation in the presence of molten deposits which produce liquid-phase corrosion of the alloys. Fireside corrosion can result in general mass loss or the formation of cracks which then allow failure by mechanical mechanisms such as fatigue [1]. Liquid-phase corrosion results in rapid attack. Chromium is generally considered to be the most beneficial alloying element for corrosion resistance [2, 3]. The exposure temperature and the type of deposit will determine the type of corrosion, which will occur. In the temperature range typically of interest (650–750 °C), alkali iron trisulfates have been considered to be the main contributor to fireside corrosion. This is due to the fact that they have melting points below the temperature range of interest, they are highly reactive, and they have been found in areas of corrosion [4]. However, recent studies indicate that severe corrosion is caused by a low melting $(\text{Na,K})_2\text{SO}_4\text{-Fe}_2(\text{SO}_4)_3$ solution which forms by the reaction of a thermally grown iron oxide scale on the surface of the heat exchanger components or iron oxides from the ash with SO_3 (oxidized from SO_2) in the gas atmosphere and alkali sulfates in the coal ash which deposit on the component surface [5]. Thus, the specific trisulfate phase is not required; liquid formation can occur at lower Fe concentrations in the deposit. The amount of corrosion increases with increasing concentrations of SO_2 and alkali sulfates. The metal loss, as a function of temperature, follows a bell-shaped curve with a maximum between 650 and 750 °C. The curve may be shifted based on alloy composition, SO_2 level, and alkali content [6–8].

A previous paper [5] explained that the mechanism for fireside corrosion of chromia-forming Fe-base alloys is “synergistic fluxing” as described by Hwang and Rapp [9] for hot corrosion of Fe–Cr alloys. SO_3 migrates through the deposit to the oxide/deposit interface, and when sufficient amounts are present, it reacts with the transient Fe_2O_3 to form $\text{Fe}_2(\text{SO}_4)_3$. The dissolution of $\text{Fe}_2(\text{SO}_4)_3$ in the alkali sulfates results in melting of the deposit. The formation of the liquid salt allows dissolution and fluxing of the protective oxide scales and base metal. The protective chromia scales are disrupted by basic fluxing, which increases the local SO_3 partial

pressure and leads to acidic dissolution of the Fe_2O_3 which forms. This maintains the conditions necessary for basic dissolution of the chromia, and the cycle is able to repeat indefinitely. Inwardly migrating SO_3 can pass through the liquid salt via an $\text{S}_2\text{O}_7^{2-}/\text{SO}_4^{2-}$ exchange reaction, where it reacts with Cr in the substrate to form inward growing Cr_2O_3 and Cr-sulfide corrosion pits. There is a low p_{O_2} , high $p_{\text{S}_2}/p_{\text{SO}_2}$ ratio at the melt/alloy interface, which causes the formation of the inward growing Cr_2O_3 and Cr-sulfide pits. The external Fe_2O_3 scale will simultaneously form via a $3\text{Fe}^{2+}/2\text{Fe}^{3+}$ exchange reaction similar to that for Co during Type II hot corrosion [10]. The iron reprecipitates as an external porous (non-protective) Fe_2O_3 scale at higher p_{O_2} . The solubility of Cr_2O_3 must be less than that for Fe_2O_3 , as it reprecipitates in the melt at a shorter distance from the reaction site, which produces the observed internal corrosion pits. Once the liquid has formed and started synergistic fluxing of the base metal (propagation stage), the amount of degradation appears to be independent of alloy composition.

Heat exchanger components for coal-fired power plants must have high creep strength, thermal fatigue strength, weldability, resistance to fireside corrosion, and resistance to steam side oxidation and spallation [3]. Martensitic or ferritic stainless steels are attractive from thermal fatigue strength and cost perspectives. However, the strongest of these materials can only be used at temperatures as high as ≈ 620 °C, and even lower temperatures when fireside corrosion is being considered [11]. At higher temperatures, stronger and more advanced austenitic stainless steels or nickel-based alloys will be needed [11]. There have been major advances in high-temperature materials development including oxide dispersion strengthened (ODS) alloys, intermetallic alloys, and nickel-based superalloys. However, these alloys are still not ideal due to either their high cost, or inability to exhibit the right balance of mechanical stability, oxidation and corrosion resistance, and manufacturability. Therefore, advanced austenitic stainless steels have been a focus of recent materials development [12].

Oak Ridge National Laboratory (ORNL) has developed a family of alumina-forming austenitic (AFA) alloys for use at high temperatures in highly aggressive atmospheres [12–18]. A description of the development and the benefits of these alloys are presented in a previous paper on the effects of water vapor on the oxidation behavior of AFA stainless steels [19]. In this study, the fireside corrosion resistance of a variety of AFA alloys was evaluated in simulated combustion atmospheres with synthetic deposits to determine potential rate controlling corrosion mechanisms and to define compositional effects. The initiation and propagation stages for corrosion and the effects of varying Cr, Al, Ni, and Nb additions on corrosion resistance were examined. The results should contribute to the development of alloys with high-temperature oxidation and fireside corrosion resistance as well as strength.

Experimental Procedures

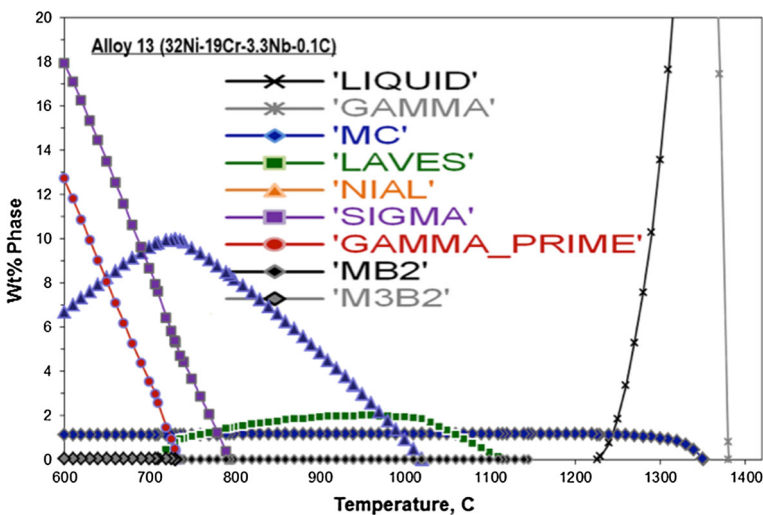
Four different AFA alloys were used for this study. The compositions are shown in Table 1. The AFA grade alloy OC4 has a combination of good oxidation resistance

Table 1 AFA alloy nominal compositions (wt%)

wt%	Fe	Cr	Al	Ni	Nb	Mn	Si	Ti	Zr
OC4	Bal.	14	3.5	25	2.5	2	0.15	–	–
OC8	Bal.	19	3	32	3.3	–	0.15	–	–
OCS	Bal.	14	3	32	3	–	0.15	2	0.3
OCT	Bal.	14	3	35	3	–	0.15	2	0.3
FeNiCr	Bal.	18	–	12	–	–	–	–	–
T92	Bal.	9	–	0.32	–	–	–	–	–

up to ~ 800 – 900 °C depending on environment and moderate creep strength via NbC-based carbide strengthening [20]. The OC8 alloy has increased chromium, nickel, and niobium concentrations and is a gamma prime strengthened alloy. This alloy has very promising strength and oxidation resistance; however, at longer times thermodynamic studies show that brittle sigma phase (and/or alpha Cr-rich phase) will form below ~ 800 °C [21]. OCS and OCT are gamma prime strengthened grade AFA alloys with lower chromium contents, designed to maintain oxidation and corrosion resistance while avoiding the undesirable sigma and/or alpha Cr-rich phase [22].

The alloys were cast, solutionized, hot rolled, and re-solutionized near 1100 – 1200 °C and then air or water quenched [21, 22]. The initial stages of this study were performed on as-processed specimens. Thermodynamic calculations show the predicted equilibrium phases in Alloy OC8 with temperature in Fig. 1 [23]. The as-processed microstructure is shown in Fig. 2 and consists primarily of austenite which contains Laves phase, $(\text{Fe,Ni})_2\text{Nb}$, and NbC. In order to examine the effect of a slowly equilibrated microstructure, specimens of OC8, OCS, and OCT were vacuum-encapsulated in quartz tubes with argon and aged 2350 h. Creep

**Fig. 1** Predicted phases of OC8 as a function of temperature [22]

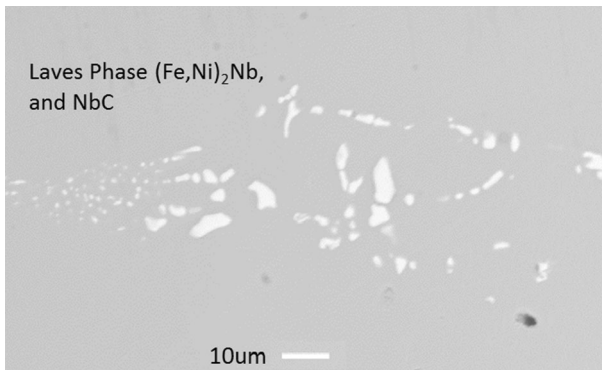


Fig. 2 Microstructure of OC8 in the as-processed state

specimens were provided by ORNL. These OC8 specimens were from a 7000-h creep test at 650 °C, OCS specimens from a 5000-h creep test at 750 °C, and OCT specimens from a 5500-h creep test at 750 °C. These equilibrated microstructures contained NiAl and Ni₃Al phases in addition to the phases present in the as-processed microstructures. In the case of OC8, sigma phase and small amounts of α -Cr were also present on alloy grain boundaries. Specimens were cut from the gage portion, which experienced loading, and the head section, which experienced the thermal conditions but not the loading. No difference was observed in microstructure or corrosion behavior.

The alloys were cut into rectangular coupon specimens approximately 14–16 mm \times 8–13 mm \times 2–4 mm. All of the specimens (both as-processed and aged) were polished to a 1200 grit SiC finish, ultrasonically cleaned in isopropanol, and dried and weighed before any deposits were applied.

Two different deposits were used in this study. The first has a composition of Na₂SO₄/K₂SO₄ in a 1:1 molar ratio and was designated M1. This deposit will remain solid at the exposure temperature (700 °C) until it reacts with sufficient thermally grown iron oxide and SO₃ from the gas atmosphere to form a low melting (Na,K)₂SO₄-Fe₂(SO₄)₃ solution. The second deposit has a composition of Na₂SO₄/K₂SO₄/Fe₂O₃ in a 1.5:1.5:1.0 molar ratio and was designated as the standard corrosion mix (SCM). The molar ratios for this mixture correspond to the stoichiometric coefficients of alkali iron trisulfates. This deposit is designed to form liquid alkali iron trisulfates even without the presence of thermally grown iron oxides on the specimen surface. The deposition procedure involved keeping the mixed deposits in powder form and placing them into alumina crucibles. The specimens were placed into the crucibles so that half of the specimen was covered with powder and half was not. This was done so that the effect of deposit thickness on the corrosion of the alloy could be examined.

Once the specimens had been placed in the salt mixture, they were exposed in a horizontal silica tube in a resistance-heated furnace shown schematically in Fig. 3. The specimens could be cycled into and out of the hot zone of the furnace manually using a magnet to push a silica rod, which held the specimens. The specimen holders

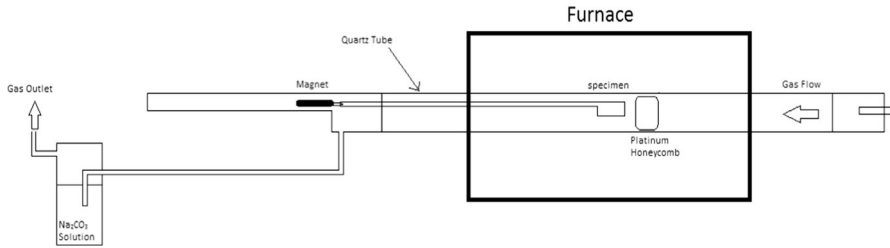
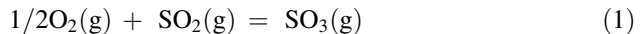


Fig. 3 Schematic diagram of the horizontal tube furnace apparatus for fireside corrosion tests

consisted of two crucibles hung by Kanthal wire below the silica rod, as shown in Fig. 4. The hot zone was maintained within three degrees of the test temperature. The gas atmospheres tested predominantly contain oxygen with varying amounts of SO_2 (100 and 1000 ppm). The gas, which was initially at room temperature, flowed into the tube at a constant flow rate of 15 mL/min (0.0125 cm/s) and passed over a platinum honeycomb catalyst placed in the hot zone of the furnace to establish the equilibrium p_{SO_3} described by Eq. (1).



The equilibrium p_{SO_3} values for the temperature and gas atmospheres tested are given in Table 2. The alloys in Table 1 were exposed to $\text{O}_2 + \text{SO}_2$ with each of the different deposits described earlier for durations typically of 20, 40, 80, and 160 h. The specimens were metallographically prepared for examination with oil instead of water to preserve the water soluble corrosion products.

The extent of the attack on the specimens was analyzed from weight change measurements and metal loss calculations. The procedure for determining the amount of metal loss follows draft ISO standards [24]. This is done by measuring the thickness of intact metal remaining in cross-sectional images and subtracting from the initial metal thickness and then dividing by 2 to obtain the metal loss of one surface. The thickness and compositions of the corrosion products along with the metal loss calculations give a better understanding of the amount and type of degradation, which occurred. Macroscopic and microscopic images and spot scan EDS analysis using a JEOL JSM-6610LV scanning electron microscope obtained from each test were used to determine the composition and morphology of the corrosion products. The different duration experiments provide information on the corrosion kinetics.



Fig. 4 Modified silica rod for crucible fireside corrosion tests

Table 2 Equilibrium SO₃ partial pressures at 700 °C

	O ₂ + 100 ppm SO ₂	O ₂ + 1000 ppm SO ₂
SO ₃ partial pressure	7.61×10^{-5} atm	7.61×10^{-4} atm

Results and Discussion

The specimens used in the initial stages of this study were in the solutionized and quenched state, and some phases are very slow to reach their equilibrium fractions. The specimens were processed near 1200 °C, and the starting microstructures of the specimens tested are characteristic of those near 1200 not 700 °C. Second phase B2-NiAl, Laves phase, carbides, and gamma prime precipitates will form rather slowly at low temperatures. The equilibration to predicted phase composition is slow, but second phases will eventually precipitate during the exposures at 700 °C. The relatively short-term exposures in the as-processed condition therefore constitute a study of the fireside corrosion resistance of the austenite matrix only and are described in the next section. Additional specimens were aged, and long-duration creep tests were conducted. The effect of the equilibrated microstructure on the corrosion resistance of these alloys will be discussed in a subsequent section.

Exposures of As-Processed Alloys

Exposures in M1

The weight change and metal loss for the as-solutionized alloys in 1000 ppm SO₂ with the M1 deposit are shown in Fig. 5. It should be noted that these mass changes may be exaggerated due to deposit adherence or scale spallation. Metal losses for the specimens were determined using ISO standards [24] and are also presented in Fig. 5. The error bars on the plot are the standard error of at least 25 metal loss measurements. For comparison, the metal loss and weight change values for the AFA alloys are compared to those for a commercial ferritic/martensitic boiler steel, T92 (nominally Fe–9%Cr–2%W) and a model austenitic alloy, Fe–12Ni–18Cr (wt%). Significant degradation occurs even after 20 h with this deposit. There was essentially no initiation stage as the weight change plot is linear and the metal loss increased very rapidly. There is a general trend of increasing degradation with time; however, some of the alloys have more rapid degradation than others. The degradation in this deposit is so rapid, and it is somewhat stochastic. Typical macrophotographs and cross-sections for OC8 with M1 are presented in Fig. 6. The corrosion products for each of the AFA alloys were similar. Thick porous external iron oxide scales grew over internal corrosion pits rich in Cr, Al, S, and O, with a sulfide-rich layer at the base of the pits. The corrosion morphologies for T92 and Fe–12Ni–18Cr were also similar albeit absent the Al. Large amounts of corrosion and metal loss occurred for each of the alloys regardless of the Cr, Al, Ni, or Nb contents. The scales from the OC4 alloy spalled. It is unknown why this is the only

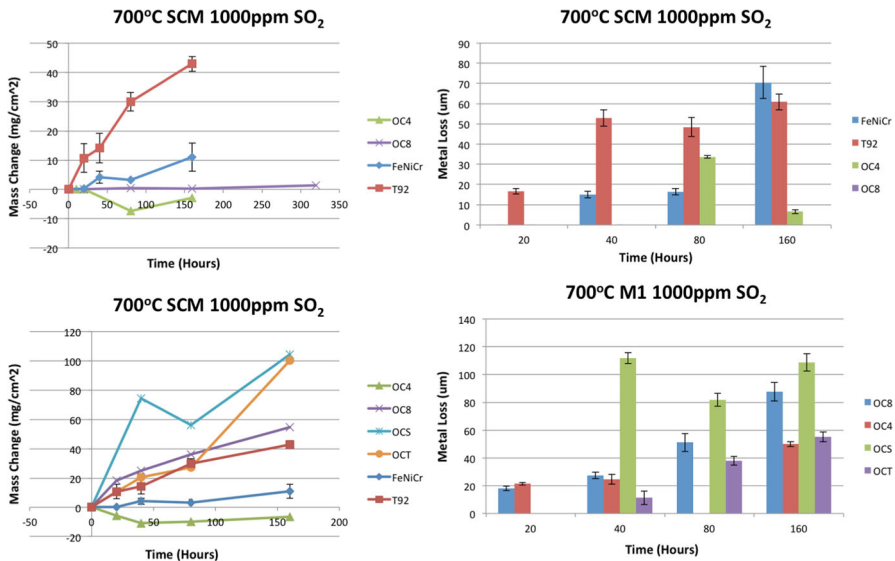


Fig. 5 Weight changes and metal loss for fireside corrosion tests at 700 °C in 1000 ppm SO₂ with the SCM and M1 deposits

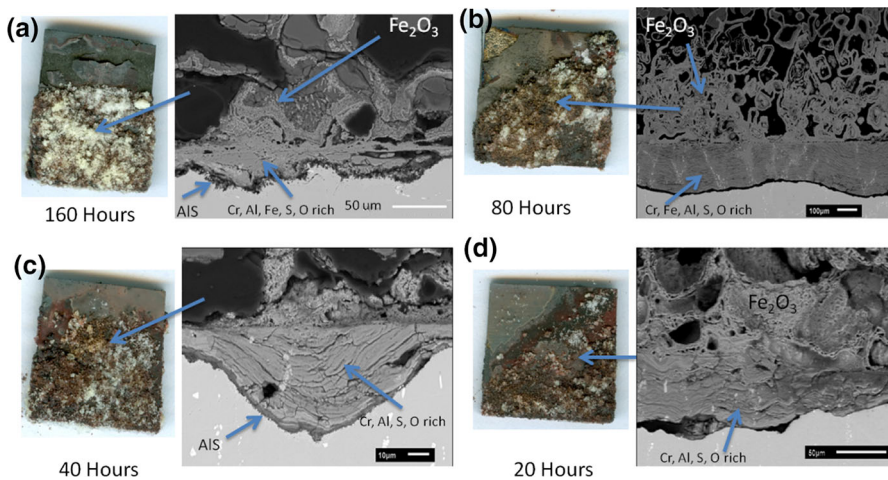


Fig. 6 Macroscopic photographs and cross-sections of OC8 after fireside corrosion at 700 °C with M1 powder in a crucible in O₂ + 1000 ppm SO₂

alloy, to exhibit spallation, and more work would be needed to determine this. The results may be summarized simply that degradation was so rapid in the M1 deposit and that protective chromia and alumina scales never formed or broke down in very short times.

Exposures in SCM

The extent of corrosion as a function of exposure time for OC4 and OC8 in the presence of SCM in $O_2 + 1000 \text{ ppm } SO_2$ can be seen in the mass change plot shown in Fig. 5. All of the alloys were corroded to a smaller extent in SCM compared to M1. The slower reaction in the SCM is attributed to saturation of the melt with Fe_2O_3 , which slows the initial disruption of the scales by synergistic fluxing [5]. The chromia- and spinel-forming alloys were significantly more degraded than the AFA alloys, particularly after 160 h. The OC4 alloy exhibited extensive attack and spallation, while the OC8 alloy performed better than any of the alloys. There was minimal if any metal loss with the OC8 alloy after all exposures, so there are no bars on the plot for this alloy. The exposure of OC8 was extended to 320 h, at which point some corrosion occurred; however, it was still minimal compared to that for the other alloys. There was some metal loss for the OC4 alloy after 80 and 160 h, as shown in Fig. 5. OC4 lost weight after only 40 h due to spallation. OC8 had very small weight gains, which were significantly lower than any of the alloys tested, even after 320 h. The initiation stage for this alloy is much longer as the result of its composition. There is a higher chromium content in OC8, which is contained in the austenite for the as-solutionized alloy. This extends the initiation period for accelerated corrosion by promoting Al_2O_3 formation via the third-element effect. OC8 also contains more Nb and Ni, which, along with Cr, have been shown to promote Al_2O_3 formation in these alloys [12–18] although the exact mechanism is unclear. Continuous Al_2O_3 formation delays the initiation of synergistic fluxing of the base metal.

Surface and cross-sectional images of OC4 after 20 and 160 h are shown in Fig. 7. Where there was no deposit, thin Fe-, Cr-, Al-rich oxide scales grew on the surface. (Identified by EDS) The spallation occurred between 40 and 80 h, which is consistent with the weight change plots. After 20 and 40 h, the oxide scales remained intact (there is a small black gap between the corrosion products and the base metal specimen which formed upon preparation for characterization). The iron

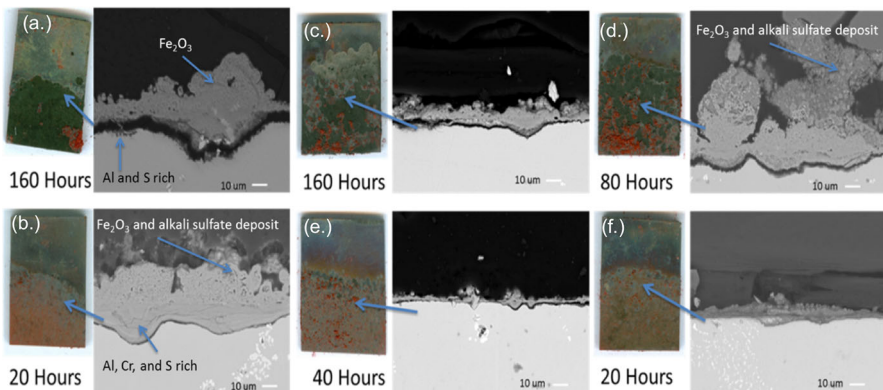


Fig. 7 Macroscopic photographs and cross-sections of OC4 after fireside corrosion at 700 °C with the standard corrosion mix powder in a crucible in **a, b** $O_2 + 1000 \text{ ppm } SO_2$ and **c–f** $O_2 + 100 \text{ ppm } SO_2$

oxide scales and corrosion pits can be seen in some areas of the thin deposit zone (the area where the deposit powder first starts to cover the specimen) after 20 h. The corrosion starts in the thin deposit zone and progresses down to the thicker deposit zone. Surface and cross-sectional images of the thick deposit zone after 20 h showed the presence of iron oxides on the surface along with alkali sulfates. The liquid $(\text{Na,K})_2\text{SO}_4\text{-Fe}_2(\text{SO}_4)_3$ solution allows for the attack on the surface of the alloy, and corrosion pits appear to be just forming. This is shown in Fig. 8. After 80 h, external iron oxides scales grew and mixed in with deposit remaining over pits rich in Cr, Al, Ni, S, and O. The aluminum and sulfur content increases with depth into the pits with a layer rich in Al, Cr, and S at the base of the pits. The largest amount of pitting occurred in some areas where the Nb-rich Laves phase or Nb-rich carbides intersected the surface. The degradation after 160 h was very similar to that after 80 h. The metal loss plot indicates there is more degradation after 80 h, but this is likely because these times are in the range where corrosion accelerates. Figure 7 also presents the results from exposure of OC4 to $\text{O}_2 + 100$ ppm SO_2 . The initiation of rapid corrosion occurs later in this gas, and the extent of corrosion after 80 h is similar to that after 40 h in $\text{O}_2 + 1000$ ppm SO_2 .

Cross-sectional images of OC8 exposed to $\text{O}_2 + 1000$ ppm SO_2 are shown in Fig. 9a. There was no measurable corrosion between 20 and 160 h. Very thin oxide scales, which were rich in Fe, Cr, and Al, grew in the non-deposit and deposit zones. Most of the alumina is present in a protective alumina layer. There was no spallation as occurred for the OC4 alloy, but corrosion pits did form in the thin deposit zone. This alloy only showed measurable corrosion after 320 h. The corrosion products were similar to those formed on OC4 after shorter times, with an external iron-rich oxide scale and internal pits rich in Cr, Al, S, and O. For comparison, cross-sectional images of the FeNiCr alloy with the SCM in $\text{O}_2 + 1000$ ppm SO_2 are shown in Fig. 10. The amount of degradation of this alloy is significantly greater

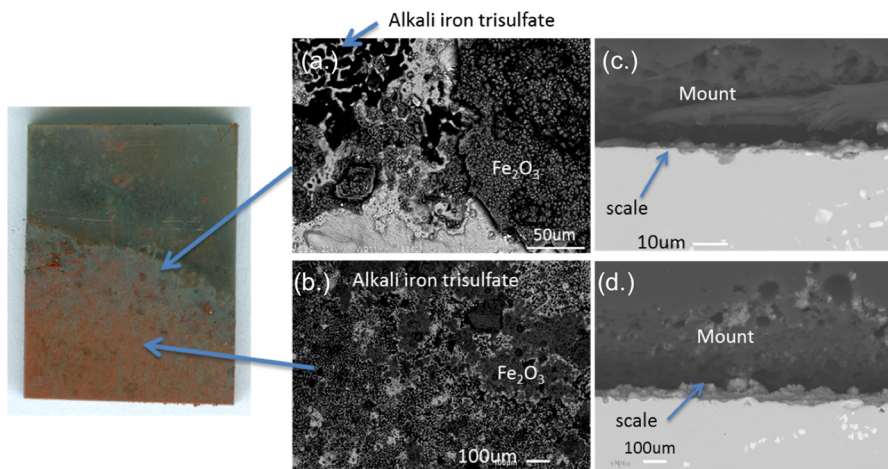


Fig. 8 Macroscopic photographs and surface micrographs (a, b) and cross-sections (c, d) of OC4 after fireside corrosion at 700 °C with the SCM powder in a crucible in $\text{O}_2 + 1000$ ppm SO_2 for 20 h

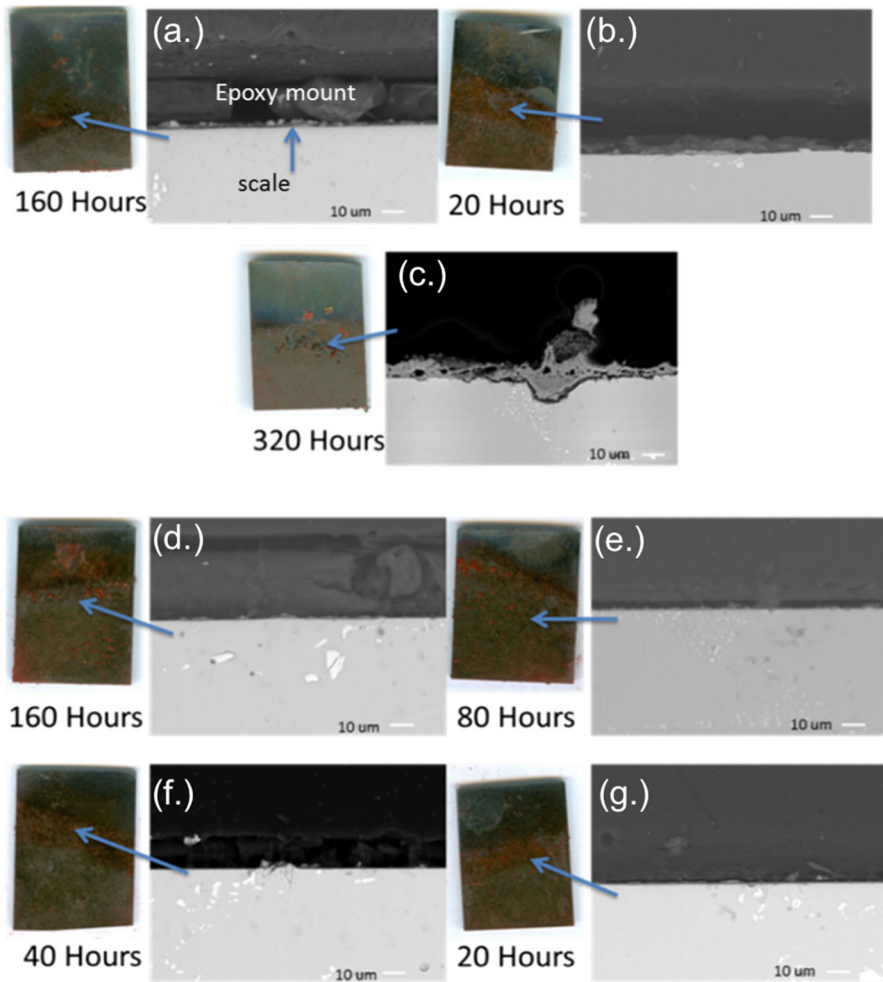


Fig. 9 Macroscopic photographs and cross-sections of OC8 after fireside corrosion at 700 °C with the standard corrosion mix powder in a crucible in **a–c** $O_2 + 1000$ ppm SO_2 and **d–g** $O_2 + 100$ ppm SO_2

than the OC8 alloy with similar Cr content indicating the importance of forming an alumina layer. Figure 9b also presents the results from exposure of OC8 to $O_2 + 100$ ppm SO_2 . As expected, there is minimal attack even after 160 h.

The alloys OCS and OCT have high nickel and niobium concentrations similar to OC8, as well as Ti and Zr additions to stabilize the high-temperature γ' - Ni_3Al strengthening phase, but they also have low chromium concentrations similar to OC4 to minimize sigma phase formation [22]. It was hoped that the higher strength OCS and OCT alloys would have sufficient fireside corrosion resistance, i.e., the benefits of Nb and Ni additions in promoting Al_2O_3 would make up for the lower chromium content. The macroscopic results of the tests on the OCS and OCT alloys in $O_2 + 1000$ ppm SO_2 are shown in Figs. 11 and 12. There was significant

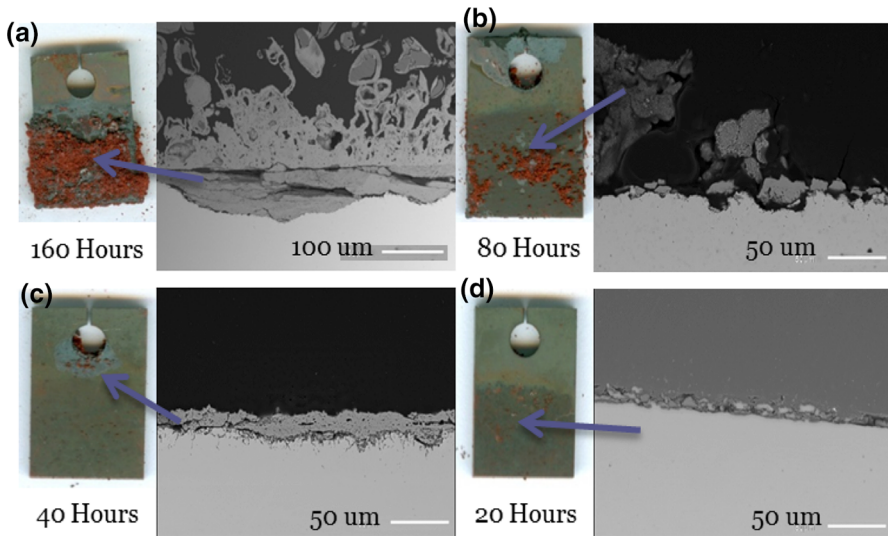


Fig. 10 Macroscopic photographs and cross-sections of Fe-12Ni-18Cr after fireside corrosion at 700 °C with the standard corrosion mix powder in a crucible in $O_2 + 1000$ ppm SO_2

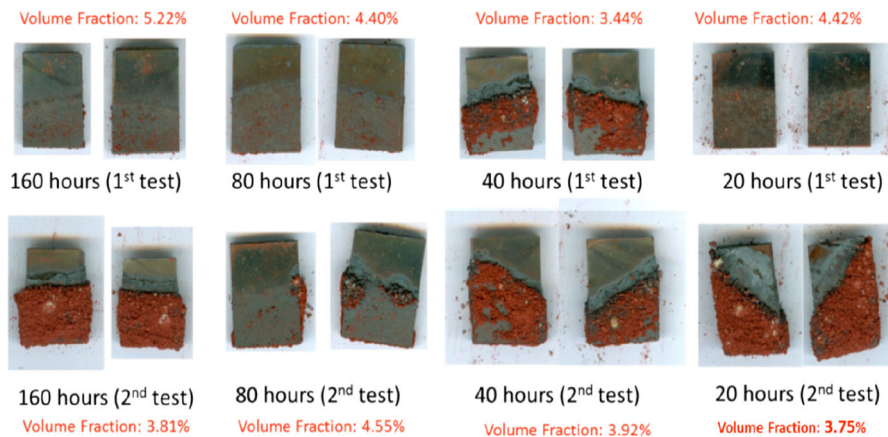


Fig. 11 Macroscopic photographs of OCS after fireside corrosion at 700 °C with the SCM powder in a crucible in $O_2 + 1000$ ppm SO_2 (volume fraction of Laves phase and NbC shown for each specimen)

variability in the results for these two alloys in duplicate tests. The cause of the variability in the results is currently unknown, but suggests these alloys have a borderline composition to exhibit the improved behavior of OC-8 over that of OC-4. Weight change and metal loss plots are not shown for these two alloys in Fig. 5 because of the large amount of variability in the results. Cross-sectional images showed that, in specimens that did not have severe corrosion, thin Fe-, Cr-, and Al-rich oxides grew on the surface. On the specimens that did show significant degradation, thick, porous, external iron-rich oxides grew over internal pits rich in

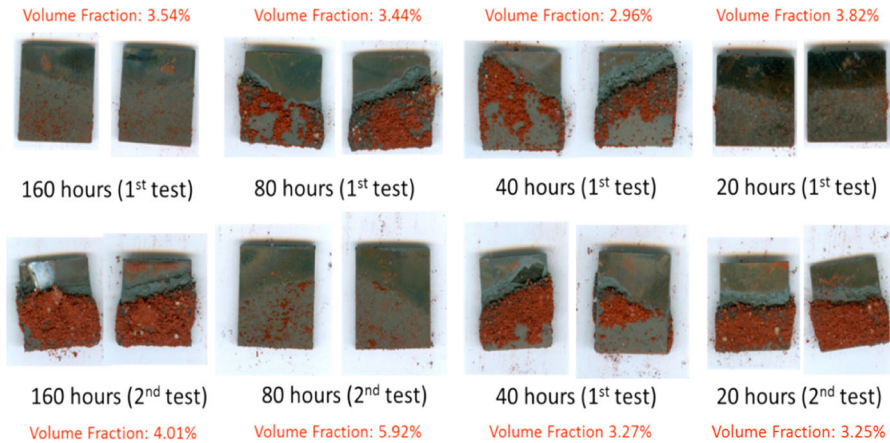


Fig. 12 Macroscopic photographs of OCT after fireside corrosion at 700 °C with the SCM powder in a crucible in $O_2 + 1000 \text{ ppm } SO_2$ (volume fraction of Laves phase and NbC shown for each specimen)

Cr, Al, Ni, S, and O with a layer of CrS and AIS at the base. Bands of NiS were also seen going through the corrosion products. The internal pits engulfed the Laves phase and carbides, which they encountered on further penetration, and these were seen in the internal corrosion products as well.

The as-processed microstructure contains significant amounts of primary $(Fe,Ni)_2Nb$ Laves phase, MC carbides, and very small amounts of NiAl. The Laves phase and MC carbides can be seen in Fig. 13. Nb- and Fe-rich oxides grow preferentially where the Laves and MC phases intersect the surface and could potentially be initiation sites for corrosion. The amount of these phases was then examined to determine whether the variability in the results was due to variability in the amount of these phases in the specimens. Measurements to determine the volume fraction of both Laves phase and Nb-carbides for many of the tested

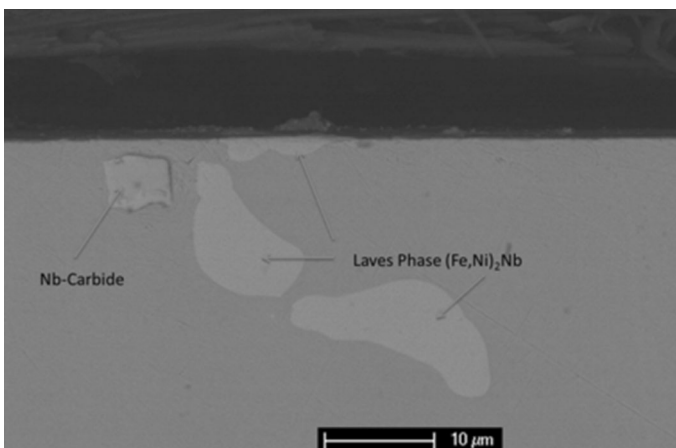


Fig. 13 Microstructure of OCT alloy in the as-processed state displaying Laves phase and Nb-carbides

specimens were performed and are shown in the macroscopic images in Figs. 11 and 12. Both Laves phase and NbC were measured together. This was done by using the GIMP photograph-editing software. The images were converted to black and white. The light Laves and NbC phases were able to be identified and separated from the rest of the image, and the area fraction of these phases was calculated for 50 random areas within each specimen cross-section. A plot of the results is also shown in Fig. 14. There was a slight correlation between the amount of Laves phase and Nb-carbides in the specimen, and the amount of degradation. Specimens containing larger quantities (more than 4%) of these phases seemed to perform better, which is the opposite of what might be expected. When these phases meet the surface of the specimen, Fe- and Nb-oxides are preferentially grown and could be a source for the liquid salt to cause corrosion more rapidly. However, when these alloys are oxidized in air and air with water vapor, Laves phases and the NbC at the surface are preferentially oxidized and then undercut by alumina, which results in no long-term detrimental effects [19, 25]. The buildup of Laves phase and NbC at the surface is therefore not initiating corrosion faster than other sites on the surface. Figures 15 and 16 show the calculated equilibrium phase fractions of the OCS and OCT alloys with temperature [21, 22]. At the temperature tested, there should be minimal Laves phase and carbides and significant amounts of gamma prime and NiAl. This was not observed, at least at SEM level imaging. The alloys were solution-heat-treated near 1200 °C and are very slow to reach their equilibrium low-temperature microstructure at 700 °C. The effect aging as the microstructure slowly changes toward the equilibrium structure on the oxidation and corrosion resistance was then examined.

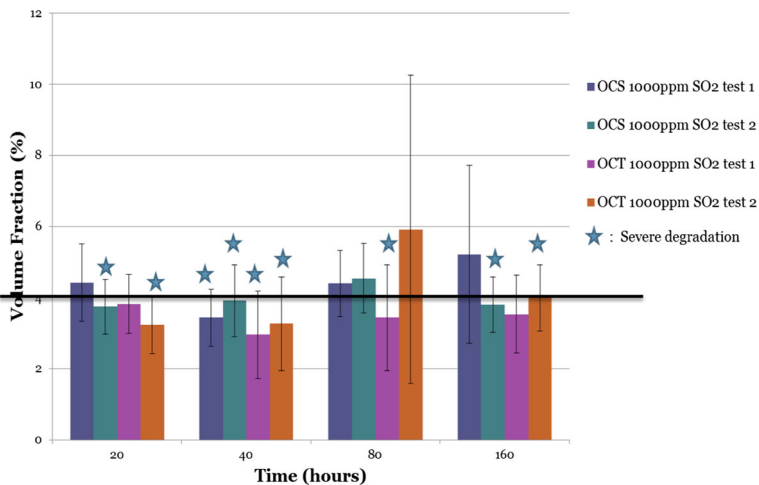


Fig. 14 Measured volume fraction of Laves phase and MC in tested specimens (*error bars* are standard error taken from a minimum of 25 calculation)

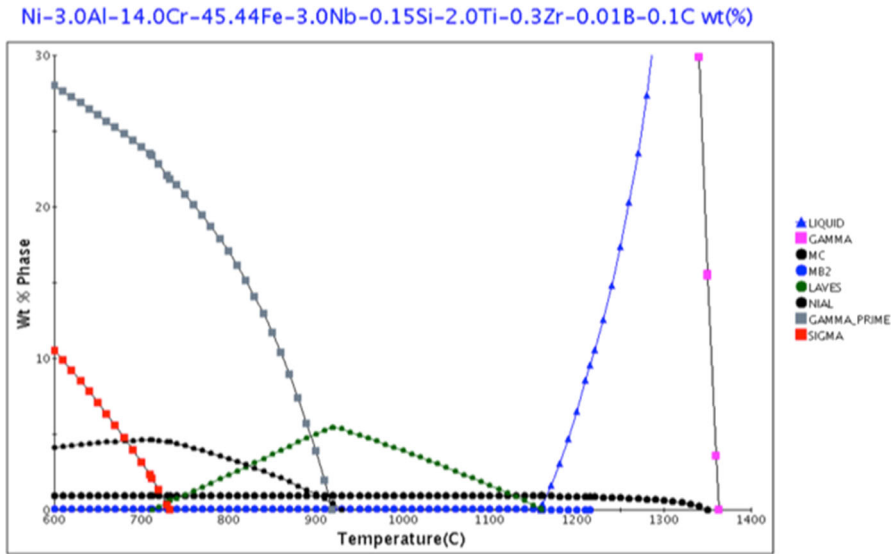


Fig. 15 Predicted phases of OCS as a function of temperature

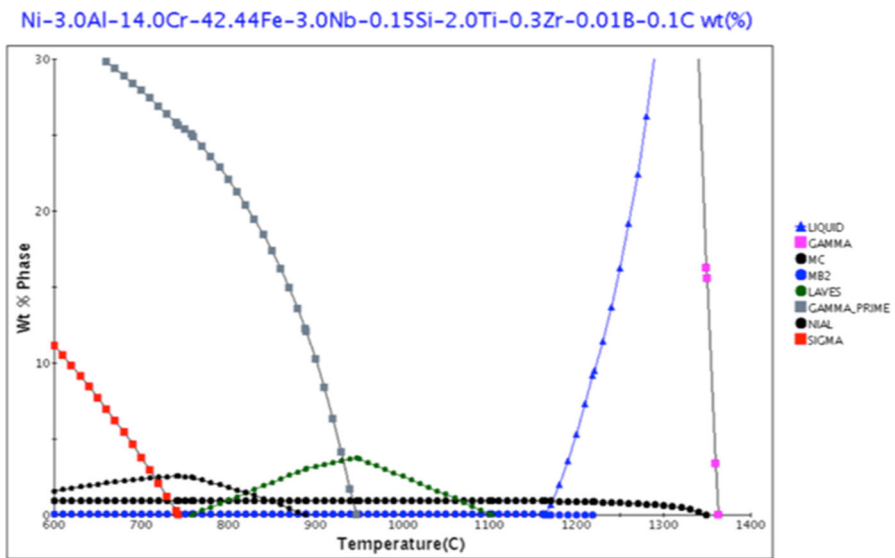


Fig. 16 Predicted phases of OCT as a function of temperature

Effect of Aging

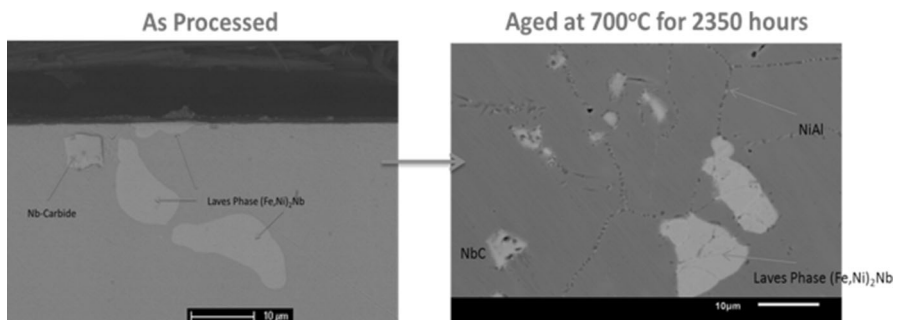
The volume fraction of Laves phase and NbC in OCS and OCT was measured before and after exposure at 700 °C in the SCM for 160 h to O₂ + 1000 ppm SO₂. The results are shown in Table 3. The amount of these phases increased for both

Table 3 Measured values of combined volume fraction (%) of Laves phase plus NbC in OCS and OCT specimens before and after exposure in the SCM for 160 h to O₂ + 1000 ppm SO₂

	OCS	OCT
Before exposure	4.25	3.81
After exposure	4.41	4.05

alloys after exposure in agreement with Figs. 15 and 16, which show that the amount of Laves phase should increase and then decrease as the alloys approach the equilibrium microstructure at 700 °C. The microstructures must be at the point in the change in which the amount of these phases increases, as they are very slowly changing into their equilibrium lower temperature microstructures. It should also be noted that neither of these specimens was severely degraded, and both ultimately contained a volume fraction of Laves phase and NbC greater than 4%. Larger amounts of NbC may mean there is less Cr tied up in carbides, allowing more Cr to be present in the austenite matrix, which may further improve the selective oxidation of Al.

The effect of the aging was examined in more detail. Specimens of OC8, OCS, and OCT were vacuum-encapsulated in quartz tubes with a small partial pressure of argon and aged for 2350 h at 700 °C. An example of the resulting microstructure of OCS (OCS and OCT are very similar alloys) is shown in Fig. 17 compared with the as-received microstructure. SEM examination indicated the presence of and Laves phase, NbC, and NiAl. If the aged specimens were at the equilibrium 700 °C microstructure, according to Figs. 15 and 16, sigma phase should also be present. The aged specimens were electrolytically etched at 1.5 V in a 10% aqueous KOH solution, which highlights the sigma phase when present. No sigma phase was detected in the aged OCS and OCT specimens. Comparison with the plot of the predicted phases in Figs. 15 and 16, with no sigma phase and still a significant amount of Laves phase present, indicates the OCS and OCT aged specimens are still not at their 700 °C equilibrium microstructures and are most likely at the microstructure predicted around 800–900 °C.

**Fig. 17** Microstructure of OCS as-processed and aged at 700 °C for 2350 h

The aged OCS and OCT specimens were then exposed at 700 °C in the SCM for 160 h to $O_2 + 1000$ ppm SO_2 . The results are presented in Figs. 18 and 19. The specimens were not severely degraded. Thin alumina scales with overlying transient oxides containing Cr and Fe grew in the non-deposit zone. The Laves phase or NbC preferentially oxidized to form Fe- or Nb-rich oxides where they intersected the surface. In the thin deposit zone, there were some areas where thicker iron oxides scales grew above small pits, which were rich in Cr, S, and O with some internal sulfidation at the base. These areas were small and the extent of the corrosion was not very severe. In the thick deposit zone, some thicker iron oxide scales grew, but there was no significant corrosion. The amount of Laves phase and NbC was noticeably increased in the aged specimens compared to the as-processed microstructure in agreement with the diagrams in Figs. 15 and 16 as the alloys reach their lower temperature equilibrium microstructure. There was also a buildup of the Nb-rich phases toward the surface of the specimens. This can be seen in the cross-sectional images in Fig. 19. The enrichment of Nb-rich Ni_3Nb toward the surface and enrichment below the oxide scale in Alloy 625 exposed to steam atmospheres at temperatures of 700–800 °C was also been reported by Garcia-Fesnillo et al. [26]. They described the enrichment beneath the surface as due to a Cr depletion below the surface from continuously forming a protective Cr_2O_3 scale, which causes a Nb depletion in the subscale zone, since Nb activity decreases with

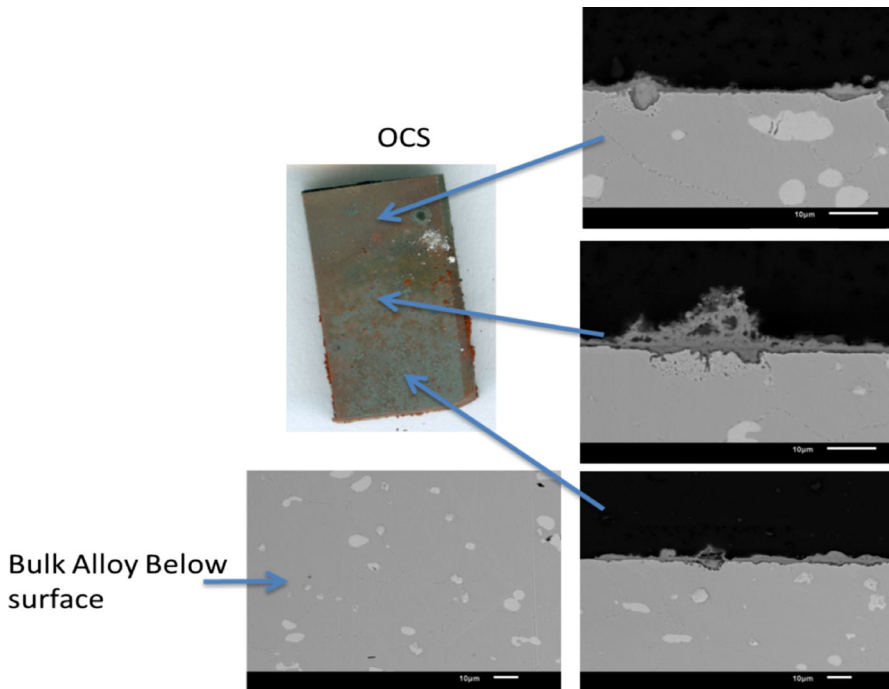


Fig. 18 OCS aged 2350 h at 700 °C and then exposed at 700 °C with the SCM powder deposit to $O_2 + 1000$ ppm SO_2 for 160 h

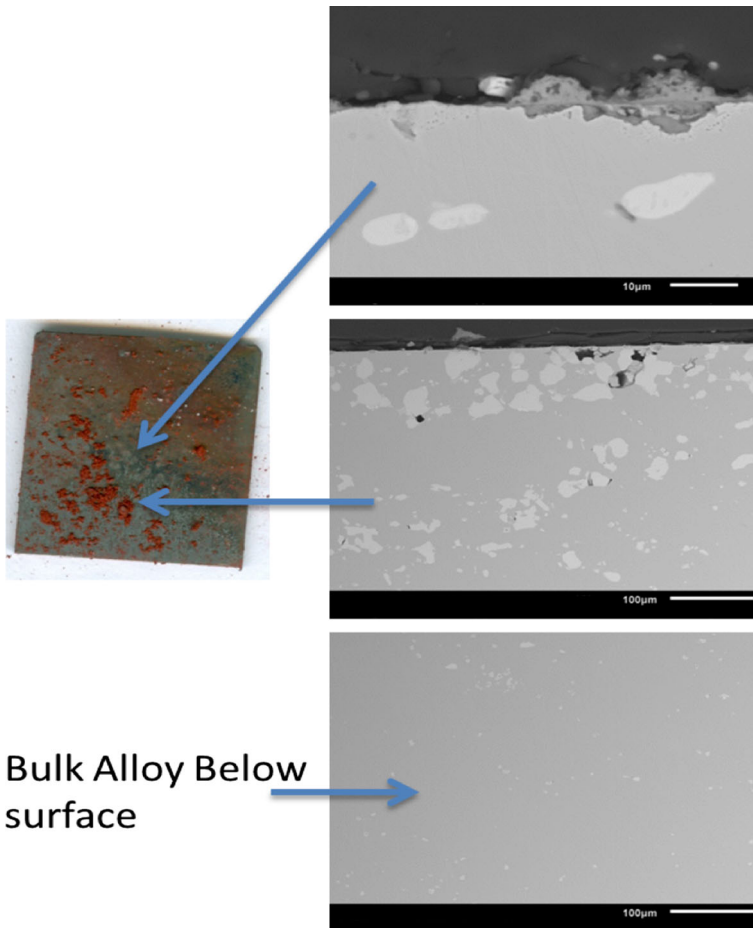


Fig. 19 OCT aged 2350 h at 700 °C and then exposed at 700 °C with the SCM powder deposit to $O_2 + 1000 \text{ ppm } SO_2$ for 160 h

Cr content. Because of the decreasing Cr content near the surface, Nb exhibits uphill diffusion toward the Cr-depleted zone, which causes an enrichment of Ni_3Nb . A similar effect was also seen for the enrichment of Laves phase at the oxide/metal interface in ferritic steels in steam atmospheres at 800 °C [27]. The enrichment of the Laves phase was once again due to a decreasing Cr content in forming a continuous oxide scale and subsequent decreasing Nb activity in this region, which leads to Nb migration to the areas of lowest Cr content. This is likely what is occurring with the AFA alloys in this study via a combination of Cr and Al depletion to form the protective oxide scale. As time increases, Al is depleted from the matrix to form a protective aluminum oxide scale and chromia is depleted by formation of transient oxide. The effects in the Ni-based alloy are more severe than would occur in a ferritic or austenitic steel due to a greater effect of the Cr content on Nb activity [27]. There were not significant amounts of degradation with the

aged OCS and OCT specimens, and the large buildup of Laves phase and NbC at the surface as well as the correlation seen previously between higher volume fractions of these phases increasing corrosion resistance indicates that these phases are affecting the corrosion mechanism by varying the Cr and Al content in the matrix such that protective alumina forms more readily.

The as-processed OC8 alloy displayed excellent corrosion resistance in the SCM deposit. However, at long durations, thermodynamic studies predict that it will form brittle sigma phase as seen in Fig. 1. The as-processed microstructure (Fig. 2) contains Laves phase, $(\text{Fe,Ni})_2\text{Nb}$, and NbC. The corrosion resistance of the alloy was excellent with the SCM in its as-processed form, but the microstructure after it has slowly changed to its equilibrium lower temperature microstructure affects its long-term corrosion resistance. An SEM image of the microstructure of the OC8 specimen after it was aged at 700 °C for 2350 h is shown in Fig. 20. It contains some Laves phase, NbC, and NiAl at the grain boundaries. The aged specimen was etched in the same manner as the other aged alloys, and a small amount of sigma phase was detected at the grain boundaries (Fig. 21). The microstructure is that which would be predicted at a temperature around 750–800 °C, which indicates a similar rate of change as observed for OCS and OCT. The aged OC8 specimen was exposed at 700 °C with the SCM powder deposit to $\text{O}_2 + 1000 \text{ ppm SO}_2$ for 160 h. The results are shown in Fig. 22. The corrosion products are similar to what was described in the As-Processed Alloys section in the M1 deposit. Thick porous external iron oxide scales grew over internal corrosion pits rich in Cr, Al, S, and O, with a sulfide-rich layer at the base of the pits. The specimen was severely corroded, and it is evident that there is a large amount of metal loss (average = 99.96 μm). Figure 23 shows that the metal loss for aged OC8 is significantly larger than that for a FeNiCr model alloy of similar Cr concentration (Fe–12%Ni–18%Cr). This is in stark contrast to the results of the as-processed specimen shown in Fig. 5 (average = 0 metal loss). The fact that this alloy is much more degraded than an

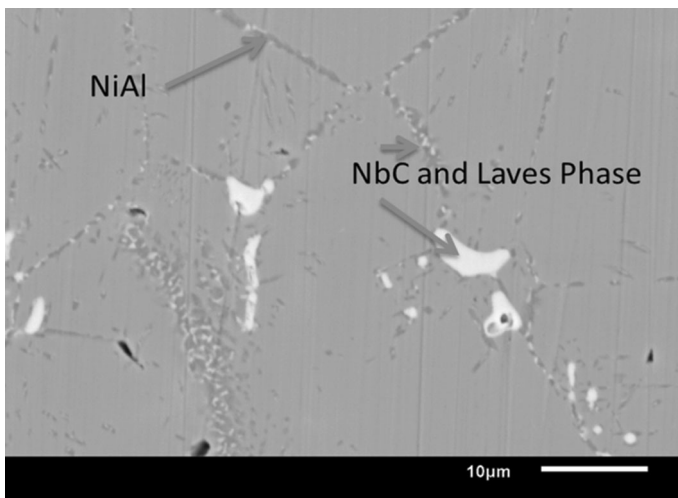


Fig. 20 OC8 aged 2350-h microstructure

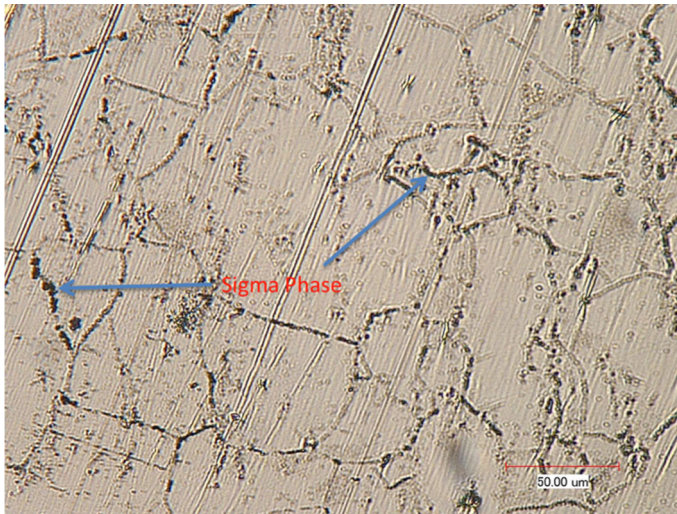


Fig. 21 Etched microstructure of OC8 aged 2350 h at 700 °C displaying sigma phase formation at the grain boundaries

alloy of similar Cr composition, suggests that the changed microstructure has significantly decreased the corrosion resistance of the alloy. The important change in the microstructure is the appearance of sigma phase. Sigma phase is a sluggishly forming, intermetallic phase, which is undesirable for its brittle nature, and it has a tendency to draw chromium from the austenite matrix. The formation of sigma phase in the aged OC8 is removing chromium from the austenite matrix, so there is less available to form a protective aluminum oxide scale on the surface via the third-element effect. The predicted change in Cr composition and Cr activity for OC8 with temperature is shown in Fig. 24 and Table 4 [23]. The Cr content in the austenite matrix does not significantly decrease when the microstructure changes from its as-processed microstructure to its equilibrium lower temperature structure. The aged OC8 alloy had a microstructure, which was characteristic of that at a temperature around 750–800 °C. At these temperatures, the austenite matrix should have sufficient amounts of Cr (19.82–20.6 wt%) to produce a protective alumina scale via the third-element effect. The sigma phase is removing Cr from the austenite, but not an amount, which would cause the increase of corrosion, which occurred and the large change from the corrosion resistance in its as-processed state. The change in Cr activity is more marked. There is an increase in the Cr activity in the austenite matrix as the microstructure changes, which may be affecting the decrease in corrosion resistance. The fact that the sigma phase forms at the grain boundaries is likely more important. The grain boundaries would be expected to be high in chromium, as they provide rapid-diffusion paths for protective Cr to reach the corrosion front, especially at these relatively low corrosion temperatures where alloy grain boundary transport is important. Sigma phase forming at the grain boundaries ties up this chromium, preventing faster diffusion to the corrosion front and locally reducing the amount of Cr available to promote alumina formation.

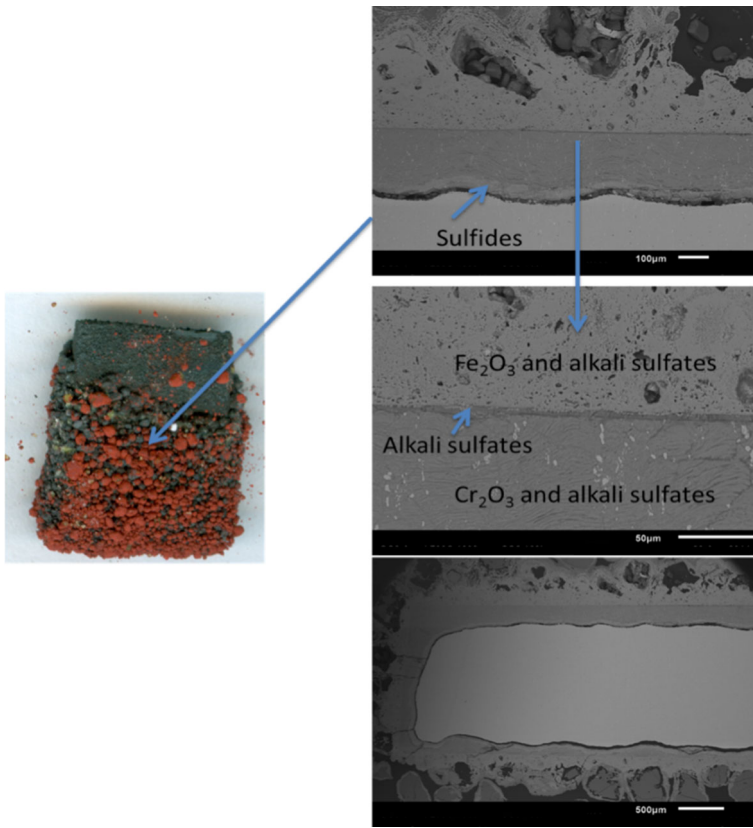


Fig. 22 OC8 aged 2350 h at 700 °C exposed at 700 °C with the SCM powder deposit to O₂ + 1000 ppm SO₂ for 160 h

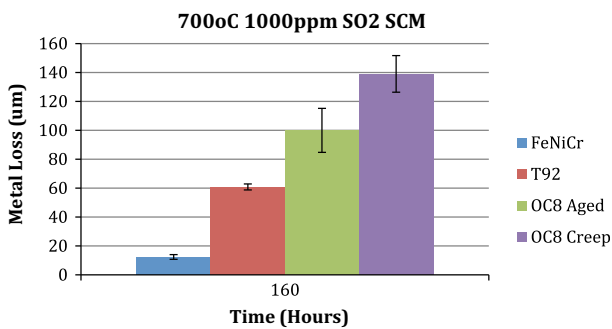


Fig. 23 Comparison of the extent of corrosion of OC8 aged for 2350 h and OC8 7000-h creep test specimen with that for the FeNiCr model alloy and T92

Specimens of OC8, OCS, and OCT exposed in creep tests for longer durations were also examined. Specimens from the gage portion, which experienced loading, and the head section, which experienced the thermal conditions but not the loading,

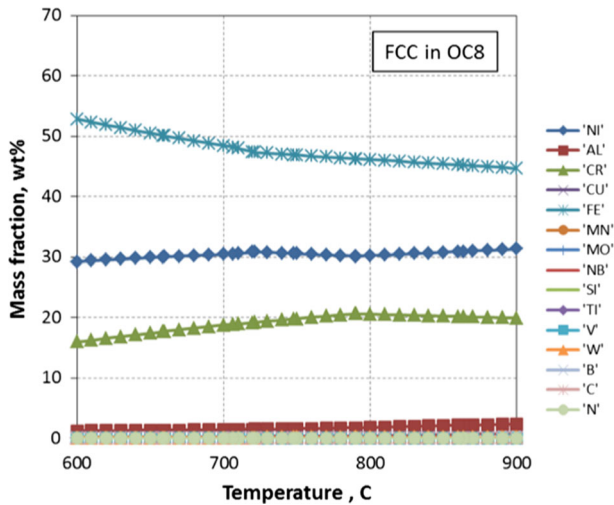
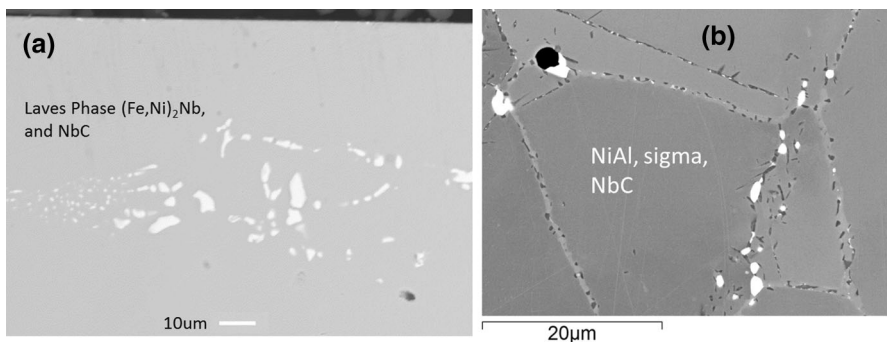


Fig. 24 OC8 austenite phase composition change with temperature [23]

were prepared and were observed in corrosion behavior. The microstructure of OC8 specimens from a 7000-h creep test at 650 °C is shown in Fig. 25 compared with the as-processed microstructure. The as-processed microstructure is representative of the predicted phases at 1100–1200 °C (Fig. 1), the temperature at which the alloy was processed. Laves phase and NbC are evident. The 7000 h creep specimen at 650 °C is more representative of the microstructure predicted at that temperature. The microstructures of specimens cut both from the gage section (deformed) and shoulder section (undeformed) were characterized in collaboration with the Forschungszentrum Juelich in Juelich, Germany [28]. The phases present were identical for the two specimens and were essentially those predicted by thermodynamic calculation. A typical micrograph, with corresponding x-ray maps, is presented in Fig. 26. Significant amounts of sigma phase, NbC, and NiAl were detected. EDS analysis by TEM indicated the major phases on the grain boundaries were NiAl and sigma (approx. comp. in at.% 49.3Cr–44.4Fe with traces of Ni and Nb). Small amounts of α -Cr (approx. comp. in at.% 76Cr–23Fe with traces of Ni and Nb) were also detected. After 7000 h, the microstructures are finally close to their equilibrium low-temperature state. These specimens were then exposed at 700 °C with the SCM to O₂ + 1000 ppm SO₂ for 160 h. The results are shown in Fig. 27. The amount of corrosion and metal loss was significant (average = 139.05 μ m), and similar to that seen with the aged specimen discussed previously. The amount of metal loss was greater with the creep specimen than with the aged specimen (Fig. 23), indicating that as more sigma phase has formed, the corrosion resistance has decreased. The sigma phase that has formed at the grain boundaries has locally decreased the amount of chromium there. The grain boundaries act as diffusion paths for chromium to reach the surface, and it is being tied up in the sigma phase. Chromium is prevented from reaching the surface to provide corrosion protection by promoting alumina formation via the third-element

Table 4 OC8 Cr content and Cr activity change with temperature [23]

Temperature (°C)	Cr content (wt%)	Cr activity
900	19.9117	0.645936
890	19.98499	0.655001
880	20.05749	0.66435
870	20.12919	0.673996
863.63699	20.17439	0.680293
860	20.2	0.683944
850	20.26987	0.694206
840	20.33897	0.704808
830	20.40726	0.715766
820	20.47475	0.727096
810	20.54143	0.738816
800	20.60727	0.750944
790.45132	20.66936	0.762925
790	20.6601	0.763106
780	20.4538	0.767184
770	20.24568	0.771402
760	20.03579	0.775764
750	19.82416	0.780278
748.10129	19.78378	0.781152
740	19.61312	0.785042
730	19.40024	0.789958
721.33475	19.21378	0.794324
720	19.18936	0.794815
710	18.99445	0.797922
706.71382	18.92571	0.7987
700	18.76569	0.801434

**Fig. 25** OC8 as-processed microstructure (a) compared with 7000-h creep at 650 °C specimen microstructure (b)

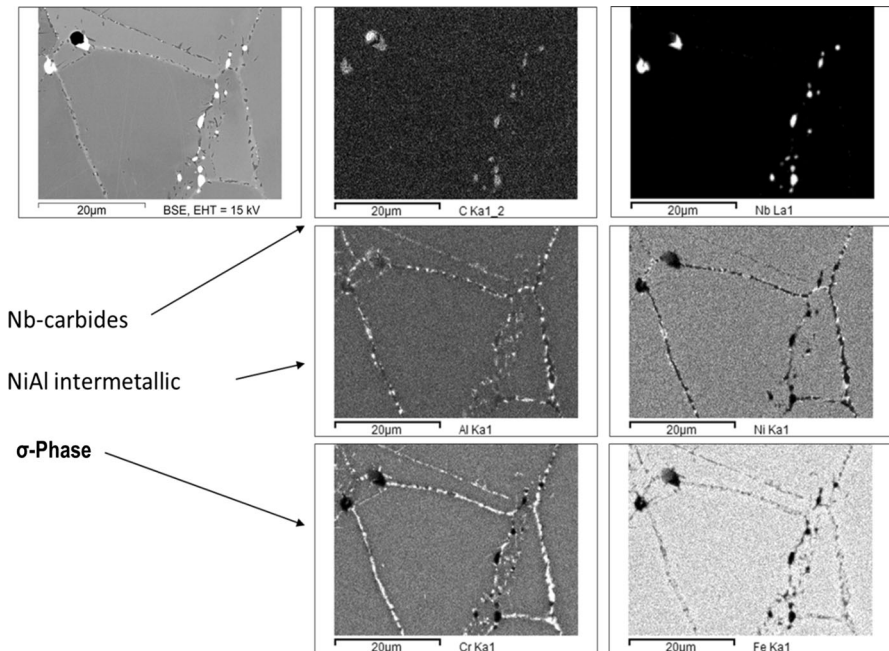


Fig. 26 Phase maps of OC8 7000-h creep specimen at 650 °C

effect. The sigma phase depletes the beneficial effects of chromium and therefore decreases the fireside corrosion resistance of this alloy.

The microstructures of OCS and OCT 750 °C creep specimens were examined by SEM and that for OCS is compared with the as-processed microstructure in Fig. 28. The creep specimen has noticeable increases in NbC and Laves phase as well as NiAl, characteristic of the microstructure that would be predicted at 750 °C (Fig. 15). The specimens were etched in order to examine if sigma phase had formed, and the results indicate none had formed. The predicted phases for these alloys from Figs. 15 and 16 confirm that at 750 °C sigma phase would not be expected to form. These specimens were also exposed at 700 °C with the SCM to O₂ + 1000 ppm SO₂ for 160 h, and the results are shown in Fig. 29. There was not a significant amount of degradation. (The metal losses for these specimens were too small to appear in Fig. 23.) There were some areas where thick iron oxide grew on the surface and some internal pits, but they were small. Where Laves phases and the NbC intersected, the surface Fe- and Nb-rich oxides grew. The fact that these specimens were not seriously degraded and that they did not have any sigma phase formation supports the previous results with the OC8 alloy that sigma phase formation at the grain boundaries decreases the corrosion resistance of the alloy by tying up chromium that would otherwise be used in selective oxidation of an alumina scale via the third-element effect. The specimens likely also were more resistant due to a noticeable increase in the amount NbC and Laves phase in the specimen and near the surface, which was explained previously. Nb was strongly

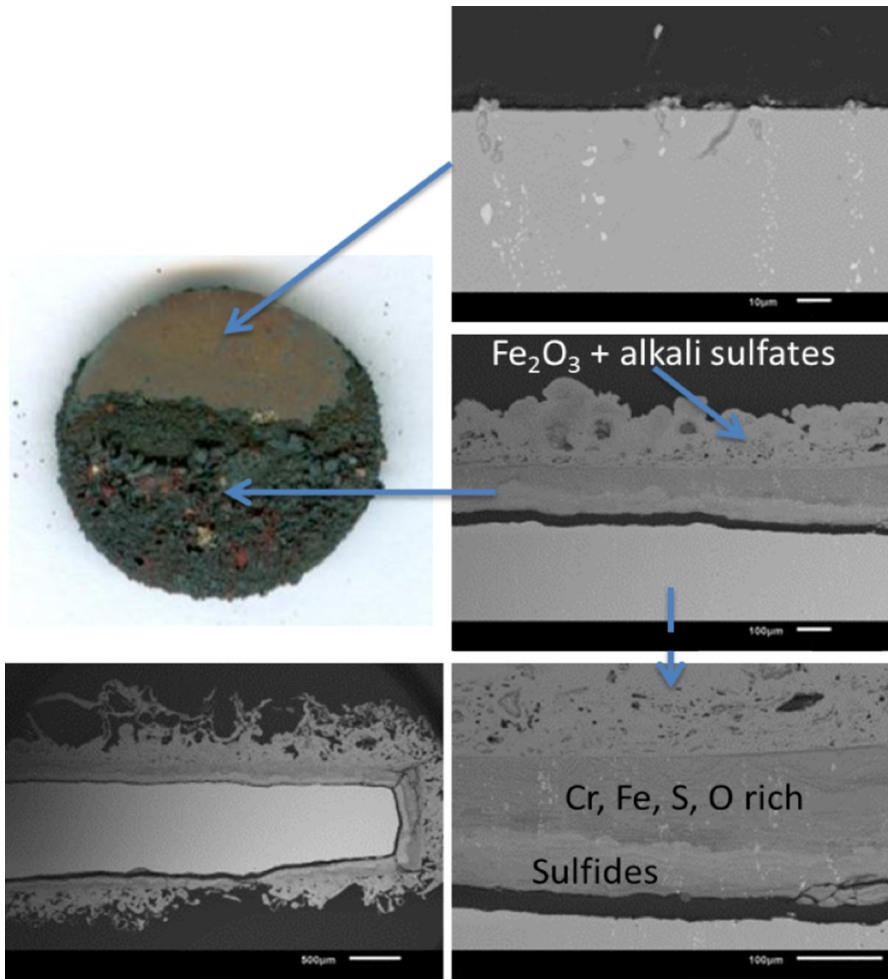


Fig. 27 OC8 7000-h creep specimens exposed at 700 °C with the SCM to O₂ + 1000 ppm SO₂ for 160 h

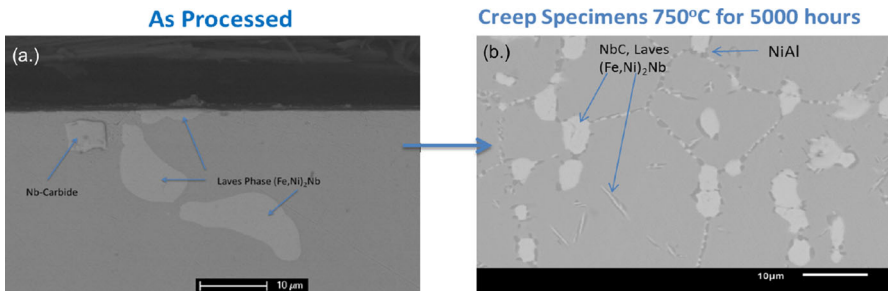


Fig. 28 a As-processed and b OCS 5000-h creep specimen microstructures

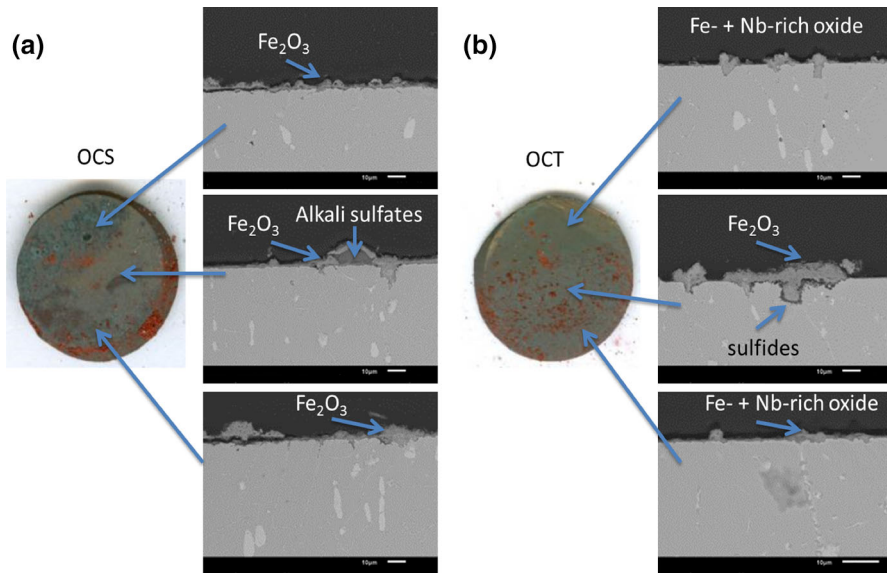


Fig. 29 **a** OCS 5000-h and **b** OCT 5500-h creep specimens exposed at 700 °C with the SCM powder deposit to O₂ + 1000 ppm SO₂ for 160 h

related to better alumina formation, although the mechanism is not completely understood. These results are consistent with the alloy design trends that show better AFA oxidation resistance/higher temperature alumina capability, with higher Nb content added to the alloy, which increases Laves and NbC and also impacts partitioning of Cr to the austenite matrix phase (see Ref. 15).

Conclusions

All of the alloys studied were more severely corroded in the M1 deposit compared to the SCM deposit as the result of rapid “synergistic fluxing.” Corrosion was so rapid, and there was little effect of alloy composition on the corrosion rate.

Exposures in the SCM deposit showed a significant effect of alloy composition and microstructure. In the as-processed state, OC4 suffered severe scale spallation and was not protective, while OC8, which contains a higher Cr content, remained protective. The OCS and OCT alloys showed a large amount of variability in the results. These alloys are borderline alloys for protection in this state. Specimens with higher volume fractions of Laves phase and NbC seemed to perform better.

The AFA alloys are sluggish to reach their equilibrium microstructure at the exposure temperature. Specimens of OC8, OCS, and OCT were aged at 700 °C for 2350 h and then retested in the SCM. The OCS and OCT specimens were not significantly degraded. The microstructures were still not at the equilibrium 700 °C microstructure as significant amounts of Laves phase and NbC as well as NiAl could be seen, and no sigma phase was found. The OC8 alloy was severely degraded as

some sigma phase had formed at the grain boundaries. Sigma phase forming at the grain boundaries ties up this chromium, preventing faster diffusion to the corrosion front and locally reducing the amount of Cr available for protection via the third-element effect to form alumina.

The OC8, OCS, and OCT alloys were also subjected to longer duration creep tests (5000–7000 h) and retested in the SCM. Specimens from the gage portion, which experienced loading and thermal exposure, and the head section, which experienced the thermal conditions but not the loading, were prepared and were observed in corrosion exposures. The OC8 alloy contained significant amounts of sigma phase and was severely degraded, likely due to the sigma formation at the grain boundaries. The OCS and OCT alloys were once again not severely degraded, but at the temperature the creep tests were performed, sigma phase still does not form, further confirming that sigma phase formation in AFA alloys after longer durations (once they reach their low-temperature equilibrium microstructure) reduces corrosion resistance. There was no apparent effect of loading on the microstructures or corrosion behavior of the alloys.

The exposures with the various microstructures indicate the significance of the factor on fireside corrosion. The OC8 alloy was extremely resistant in the as-processed state but was rapidly degraded when the microstructure had been equilibrated prior to exposure. Conversely, the OCS and OCT alloys, which were borderline in the as-processed state, were quite resistant after their microstructures had been equilibrated.

The results indicate that corrosion resistance in these environments comes from alumina but the alloys need more Cr and in a very accessible microstructure location to get the third-element effect to promote the alumina.

Acknowledgements This work at University of Pittsburgh was performed in support of the National Energy Technology Laboratory's ongoing research on Advanced Combustion under RUA Contract URS-168. Carpenter Technology Corporation and Dr. M.P. Brady at Oak Ridge National Laboratory are acknowledged for supplying the AFA material. Dr. M.P. Brady and Y. Yamamoto of Oak Ridge National Laboratory is also acknowledged for helpful discussion and providing thermodynamic plots. L. Niewolek of Forschungszentrum Juelich is acknowledged for microstructural analysis of the OC8 creep specimen.

Compliance with Ethical Standards

Conflict of interest The authors declare they have no conflict of interest.

Human and Animals Rights There were no human participants or animals in this study.

References

1. J. Stringer and I. G. Wright, *Oxidation of Metals* **44**, 265 (1995).
2. N. Otsuka and R. A. Rapp, *Journal of the Electrochemical Society* **137**, 46 (1990).
3. A. U. Syed, N. J. Simms and J. E. Oakey, *Fuel* **101**, 62 (2012).
4. W. T. Reid, *External Corrosion and Deposits Boilers and Gas Turbines*, (Elsevier, New York, 1971).
5. B. S. Lutz, G. R. Holcomb and G. H. Meier, Determination of the Initiation and Propagation Mechanism of Fireside Corrosion. *Oxidation of Metals* **84**, 353 (2015).

6. M.S. Gagliano, H. Hack, and G. Stanko, *Fireside Corrosion Resistance of Proposed USC Superheater and Reheater Materials: Laboratory and Field Test Results*. Presented at the 33th International Technical Conference on Coal Utilization and Fuel Systems, 2008.
7. K. Natesan, A. Purohit, and D.L. Rink, *Fireside Corrosion of Alloys for Combustion Plants*, in *Proceedings of 16th Annual Conference on Fossil Energy Materials*, Baltimore, MD, April 22–24, 2002.
8. H. Hack and G. Stanko, *Experimental Results for Fireside Corrosion Resistance of Advanced Materials in Ultra-Supercritical Coal-Fired Power Plants*. Presented at the 32nd International Technical Conference on Coal Utilization & Fuel Systems, 2007.
9. Y. S. Hwang and R. A. Rapp, *Journal of the Electrochemical Society* **137**, 1276 (1990).
10. K. L. Luthra, *Metallurgical Transactions A* **13**, 1853 (1982).
11. R. Viswanathan, J. F. Henry, J. Tanzosh, G. Stanko, J. Shingledecker, B. Vitalis and R. Purgert, U.S. Program on Materials Technology for Ultra-Supercritical Coal Power Plants. *Journal of Materials Engineering and Performance* **14**, 281 (2005).
12. Y. Yamamoto, M. P. Brady, Z. P. Lu, P. J. Maziasz, C. T. Liu, B. A. Pint, K. L. More, H. M. Meyer and E. A. Payzant, *Science* **316**, 433 (2007).
13. M. P. Brady, Y. Yamamoto, M. L. Santella, P. J. Maziasz, B. A. Pint, C. T. Liu, Z. P. Lu and H. Bei, *JOM* **60**, 12 (2008).
14. Y. Yamamoto, M. L. Santella, M. P. Brady, H. Bei and P. J. Maziasz, *Metallurgical and Materials Transactions A* **40**, 1868 (2009).
15. Y. Yamamoto, M. P. Brady, Z. P. Lu, C. T. Liu, M. Takeyama, P. J. Maziasz and B. A. Pint, *Metallurgical and Materials Transactions A* **38**, 2737 (2007).
16. M. P. Brady, Y. Yamamoto, M. L. Santella and L. R. Walker, *Oxidation of Metals* **72**, 311 (2009).
17. M. P. Brady, Y. Yamamoto, M. L. Santella and B. A. Pint, *Scripta Materialia* **57**, 1117 (2007).
18. Y. Yamamoto, M. Takeyama, Z. P. Lu, C. T. Liu, N. D. Evan, P. J. Maziasz and M. P. Brady, *Intermetallics* **16**, 453 (2008).
19. N. M. Yanar, B. S. Lutz, M. P. Brady and G. H. Meier, *Oxidation of Metals* **84**, 541 (2015).
20. M.P. Brady, J.H. Magee, Y. Yamamoto, P.J. Maziasz, M.L. Santella, B.A. Pint, and H. Bei, *Development and Exploratory Scale-Up of Alumina-Forming Austenitic (AFA) Stainless Steels*, in *Proceedings of Stainless Steel World 2009 Conference & Expo, Maastricht*, The Netherlands, November 10–12, 2009, Stainless Steel World, The Netherlands, 2009.
21. M. P. Brady, J. Magee, Y. Yamamoto, D. Helmick and L. Wang, *Materials Science and Engineering: A* **590**, 101 (2014).
22. Y. Yamamoto, G. Muralidharan and M. P. Brady, *Scripta Materialia* **69**, 816 (2013).
23. Y. Yamamoto, G. Muralidharan, and M.P. Brady, Private Correspondence, 2013.
24. Corrosion of metals and alloys-methods for metallographic examination of samples after exposure to high temperature corrosive environments, in *Draft ISO Standard. ISO/TC 156 NWI 5092005*, 2006.
25. J.-Y. Kang, H.-Y. Ha, M.-H. Jang, J. Moon, D.-W. Suh and T.-H. Lee, *Scripta Materialia* **102**, 63 (2015).
26. L. Garcia-Fresnillo, A. Chyrkin, C. Boehme, J. Barnikel, F. Schmitz and W. J. Quadackers, *Journal of Materials Science* **49**, 6127 (2014).
27. C. Asensio, A. Chyrkin, L. Niewolak, V. Konoval, H. Hattenforf, B. Kuhn, L. Singheiser and W. J. Quadackers, *Electrochemical and Solid State Letters* **14**, 17 (2011).
28. L. Niewolek, Forschungszentrum Juelich, Germany, private communication, 2013.